

# Body Force Model for the Aerodynamics of Inclined Perforated Surfaces

Juntao Xiong,\* Andrew Johnson,† Feng Liu,‡ and Dimitri Papamoschou§  
University of California, Irvine, Irvine, California 92697

DOI: 10.2514/1.J051699

This is a joint experimental and computational research effort on the aerodynamics of perforated surfaces inclined to a freestream. The goal is to characterize the key parameters affecting the flowfield in order to construct a macroscopic computational model that obviates resolution of the detailed perforations. The model simulates the effects of the perforated surfaces by locally applying a body force term in the momentum equation. The study considers wedge-shaped deflectors used for jet noise reduction in turbofan engine nozzles in the form of flaps with varying angles and perforation shapes. The experiments measured the mean velocity field inside and in the wake of the flaps while the numerical analysis comprised direct computations of simplified perforated flaps and computations using the body force model. It is found that the effective porosity of the surface is affected by flow separation within the perforations. The flow blockage of the separation regions is primarily a function of the angle to the freestream and the ratio of the thickness to hole diameter. Accordingly, a formulation for the body force model is proposed that incorporates this finding. The resulting velocity field is in good agreement with the experiments and with the direct computations.

## Nomenclature

AR	=	perforation aspect ratio
C	=	inertial resistance coefficient
$C_D$	=	drag coefficient
$C_p$	=	pressure coefficient
D	=	hole size on plane of freestream
$F_B$	=	body force
H	=	nozzle height
h	=	flap height
L	=	flap length
$M_\infty$	=	freestream Mach number
$p_a$	=	ambient pressure
$p_0$	=	total pressure
t	=	flap thickness
$U_\infty$	=	freestream velocity
$v_n$	=	permeation velocity
W	=	nozzle width
x, y, z	=	Cartesian coordinates
$\alpha$	=	wedge half-angle
$\beta$	=	porosity (fraction of open area over total area)
$\beta_{\text{eff}}$	=	effective porosity

## I. Introduction

EXTERNAL flowfields involving perforated surfaces can be found in a variety of aerospace and industrial applications. On aircraft, perforated plates have been investigated or used primarily

for drag increase, including flaps on dive bombers [1] and speed brakes of advanced transports [2,3]. Other aeronautical applications have included lift augmentation [4,5], suppression of weapons-bay turbulence [6], and reduction of jet noise [7] as the motivation for this study. Perforated screens are also used in geophysical and civil engineering applications as wind shelters [8]. Common to all of these implementations is the benefit of the bleed air behind the plate, which suppresses large-scale turbulence, reduces structural loading, and can attenuate noise.

The computational treatment of flows through and around porous plates can be daunting if one is to resolve the flowfield of each perforation. Here we seek a macroscopic approach that will reproduce the gross-flow features without requiring resolution of the details of the perforations. We believe that such a model will be a useful design tool for many of the technologies described above. The motivator of our work has been the development of the porous wedge-shaped fan flow deflector (FFD) for the reduction of jet noise from turbofan engines [7]. However, the results will be generic enough to be applicable to a large category of devices employing normal or inclined porous plates. This section provides an overview of the treatment of normal and inclined porous plates, and presents key aspects of the aerodynamics of wedge FFDs. The following sections present the experimental and computational studies, and the resulting macroscopic computational model.

Substantial work has been done on flow through perforations inside ducts, that is, in a confined environment where all of the flow must pass through the perforation. The book by Fried and Idel'chik [9] provides an important reference for these types of flows. In the present study, we are concerned with a perforation in an external flowfield, wherein the flow has the freedom to go through and around the object. The theory and empirical correlations for perforations in ducts is not generally applicable to external flows, except possibly locally once the streamline pattern is known.

The experiments of Castro [10] represent the most prominent work on the aerodynamics of perforated plates normal to a freestream. By varying the hole diameter from plate to plate, Castro investigated a range of porosities  $\beta = 0.0$  to  $0.645$ . Two distinct flow regimes were identified: one where the wake is dominated by a vortex street at low porosity, and another where the wake is apparently free of a vortex street at high porosity. In Castro's paper [10], the drag coefficient  $C_D$  was plotted against the parameter  $1/\beta^2$ . Plotted directly against  $\beta$ ,  $C_D$  shows practically a linear decline with increasing porosity. Figure 1 reproduces this result, along with computational predictions to be discussed later. There are several experimental investigations of wind

Presented at the 49th AIAA Aerospace Sciences Meeting and Exhibit, Orlando, FL, 4–7 January 2011; received 24 October 2011; revision received 22 March 2012; accepted for publication 9 May 2012. Copyright © 2012 by D. Papamoschou and F. Liu. Published by the American Institute of Aeronautics and Astronautics, Inc., with permission. Copies of this paper may be made for personal or internal use, on condition that the copier pay the \$10.00 per-copy fee to the Copyright Clearance Center, Inc., 222 Rosewood Drive, Danvers, MA 01923; include the code 0001-1452/12 and \$10.00 in correspondence with the CCC.

\*Postdoctoral Researcher, Department of Mechanical and Aerospace Engineering; jxiong@uci.edu. Member AIAA.

†Postdoctoral Researcher, Department of Mechanical and Aerospace Engineering; adjohnso@uci.edu. Member AIAA.

‡Professor, Department of Mechanical and Aerospace Engineering; fliu@uci.edu. Associate Fellow AIAA.

§Professor, Department of Mechanical and Aerospace Engineering; dpapamos@uci.edu. Fellow AIAA.

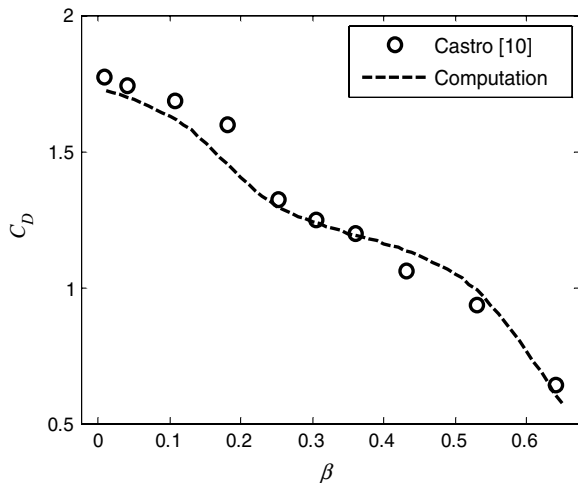


**Fig. 1 Drag coefficient versus porosity for a perforated plate normal to a freestream.**

fences [11–13], which include the effect of the incoming boundary layer and, thus, cannot be compared directly to Castro’s work [10]. Nevertheless, the existence of two flow regimes was found there also [12]. Kim and Lee [13] investigated the effect of hole diameter at constant porosity. The mean axial velocity profiles and the shear layer development appear fairly insensitive to hole diameter, although there are some changes in the transverse mean velocity and the turbulence statistics. With regard to noise impacts, we expect that the perforation will introduce acoustic fluctuations associated with the dominant noise emission from the individual jets emerging from the perforations. By making the holes small, one can shift the noise content to higher frequencies where atmospheric absorption dampens the noise level very rapidly. This was the strategy for the perforated drag plates investigated by Sakaliyski et al. [2] and the FFD porous edge investigated by Papamoschou [7].

There is very little information available on the aerodynamics of inclined porous plates. Our treatment in this section and throughout the paper will be confined to simple perforations with the hole orientation normal to the plate surface. Even under this scenario, it is easy to see that the inclination causes a complex flowpath through the holes. A significant amount of drag data for perforated inclined surfaces can be found in 1940s wartime reports on the aerodynamics of airfoils with split flaps [1]. As an example, considering split flaps at 30 deg deflection and occupying one-fifth of the chord length, the zero-lift drag coefficient decreased by 16% when the porosity increased from 0.0 to 0.331. We note that the zero-lift drag is dominated by the drag of the 30 deg flaps, so we can make a direct inference as to the drag of the perforated plates. The 16% decline is in line with Castro’s trend [10], although it is about half of what we would expect by using Castro’s data directly (Fig. 1). This suggests that the inclination angle affects the “effective porosity” of the perforation. Recently, Nedic et al. [3] conducted an aeroacoustic investigation of spoilers with fractal perforation patterns at 30 deg inclination and porosities ranging from 0.25 to 0.41. The fractal geometry is believed to alter the turbulence in the wake in a way that provides beneficial impacts on noise. Compared to a solid spoiler, the fractal spoilers reduced low-frequency noise by 2.5 dB, and they had minimal impact on lift and drag. The small change in drag again suggests that the inclination changes the effective porosity of the surface.

Defining an effective porosity for inclined perforated surfaces is at the core of our modeling effort. The schematic of Fig. 2 presents a simple heuristic model for this purpose. A plate of thickness  $t$  is inclined at angle  $\alpha$  to a freestream. The perforation holes are oriented normal to the surface and have simple shapes, such as circular, oval, or rectangular. The hole size is  $D$  on the plane of the freestream ( $x$ - $z$  plane in Fig. 2). Considering the major differences from the flow normal to a perforation, we expect the separation from the upstream corner of each hole to govern the effective area of the hole and, thus, the blockage of the perforation. Denoting the size of the separation

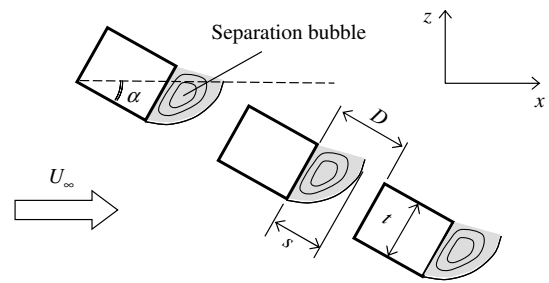


**Fig. 2 Fundamental fluid mechanics of an inclined perforated plate.**

bubble as  $s$ , for a given incidence angle, we anticipate  $s$  to grow with the thickness  $t$ . However, the bubble cannot entirely fill the hole as there will always be some flow passing through the hole. Expecting  $s/D$  to reach an asymptotic value as  $t/D \rightarrow \infty$ , we conjecture a trend of the type  $s/D \sim \tanh(t/D)$ . Further, we anticipate the effect of incidence angle on  $s$  to scale as  $\cos \alpha$ , giving  $s/D = 0$  for  $\alpha = \pi/2$  (normal incidence) and  $s/D \rightarrow 1$  for  $\alpha = 0$  and  $t/D \rightarrow \infty$ . Generalizing these observations, the conjectured trend for the size of the separation bubble is of the form

$$\frac{s}{D} = \cos^n \alpha \tanh \left[ b \frac{t}{D} \right] \quad (1)$$

with the power  $n$  and coefficient  $b$  to be determined empirically. The proposed relation does not include viscous effects that would become prevalent for  $t/D \gg 1$  or when the Reynolds number based on hole size becomes very small. Equation (1) will be the basis for a model for the effective porosity to be introduced in Sec. III.C.

Figure 3 shows the generic shape and installation of the wedge-shaped FFD. The FFD approach for reducing jet noise from turbofan engines has been the subject of past publications [7,14], so here we provide a brief overview with emphasis on the aerodynamics of the wedge-shaped deflector. The wedge sits outside the fan duct, in the vicinity of the fan exit plane, and acts as a lateral force generator to redistribute the initially annular fan exhaust so that it is thicker in the sideward and downward directions, reducing velocity gradients and production of turbulent kinetic energy in those directions. As a result, sideline and downward noise can be attenuated quite effectively, particularly in the direction of peak emission. However, the wake of a solid wedge introduces strong localized gradients between the core stream and dead-flow region in the near wake of the wedge. The resulting noise can be severe enough to compromise the acoustic benefit of the deflectors. A remedy is to allow some fan air through the wedge by perforating the wedge surfaces. In most practical applications, the wedge would be in the shape of flaps that deploy during the noise-sensitive segments of flight (mainly takeoff) and retract otherwise. Perforating the flaps is a simple engineering solution, which has demonstrated significant benefit, practically eliminating the excess noise caused by the wake [7].

To facilitate the interpretation of the results of this study, it is useful to have an overall understanding of the aerodynamics of the FFD wedge, focusing initially on the solid case. Figure 4 shows simplified sketches of streamlines and pressure distributions with comparison to the classic problem of the two-dimensional (2-D) wedge cylinder.

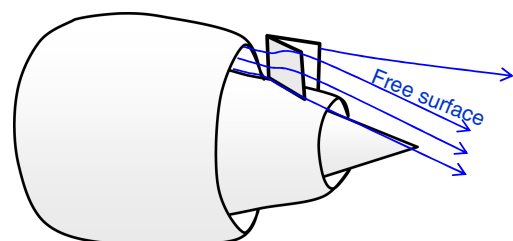


**Fig. 3 Illustration of the fan flow deflection process using a wedge-shaped deflector.**

These observations are based on past experiments and computations of the FFD wedge flow [15,16], and the experiments of Von Tanner on the drag of 2-D wedge cylinders [17]. We note that the FFD wedge acts on a flow bounded by a free surface: the shear layer between the fan stream and the ambient. This is illustrated in Fig. 4a. Because of the compression on the lower part of the wedge surface, the free surface on the upper part is deflected upward, creating an upwash. The exposure of the upper part and base of the wedge to the ambient creates a flow and pressure fields fundamentally different from those in a 2-D wedge cylinder. For the FFD wedge (Fig. 4b), the sides experience compression (starting with the stagnation point at the apex) and the base has weak suction with  $C_p \approx -0.2$ . The wake does not close (there is no recirculation region); instead the separation streamlines are directed away from the plane of symmetry, consistent with the function of the wedge as a deflector. For the wedge cylinder (Fig. 4c), the sides experience a compression followed by an expansion and the base has strong suction with  $C_p \approx -1.0$ . The net lateral force is zero, so the wake closes and forms a recirculation region. Because of the weak base suction of the FFD wedge, its drag coefficient is about 75% lower than that of the wedge cylinder [15,16].

Introducing perforations on the FFD wedge generates the desired bleed flow at the wedge base. We do not expect fundamental changes in the pressure and flowfields depicted in Fig. 4b, although the base suction will weaken further. For practical applications, we desire a macroscopic model for prediction of the mean flow through and around the wedge. This is crucial for assessing the overall aerodynamic performance of the wedge in terms of effectiveness in deflecting the fan flow and performance penalty. An additional consideration is prevention of the core stream from scrubbing the engine pylon when the wedge flaps are installed on the pylon [7]. We do not expect the macroscopic model to produce meaningful turbulence statistics that can be connected to the self-noise of the perforations. For acoustic applications, the practical guidance is to make the holes small enough that the self-noise is shifted to high frequency and attenuated by atmospheric absorption [2].

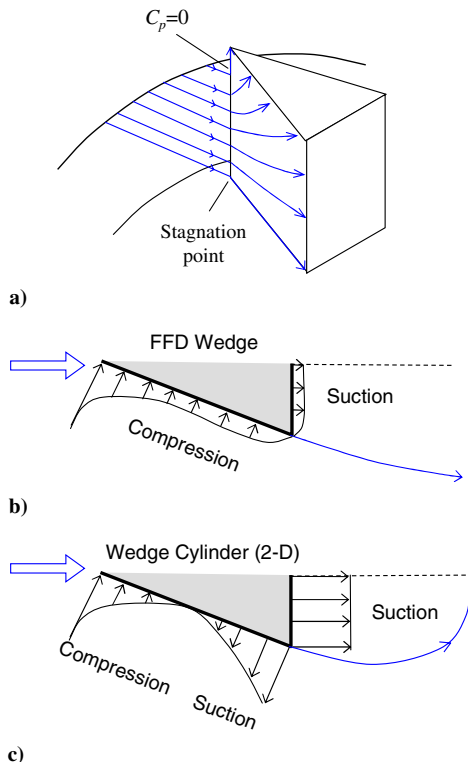


**Fig. 4** Fundamental fluid mechanics of fan flow deflector wedge: a) streamline pattern on wedge surface, b) pressure distributions and free streamline at wedge midplane, and c) comparison with wedge cylinder.

## II. Experimental Details

### A. Nozzle Apparatus and Perforations

The goal of the experiments was to provide fundamental insight into the fluid mechanics of perforated surfaces related to the FFD wedge and to validate the computational predictions. Because our jet aeroacoustics facility is of small scale (typically 1/50th scale of a full engine), the wedge dimensions on the nozzle exemplified in Fig. 3 are on the orders of millimeters. These small dimensions make the integration of instrumentation into the wedge very challenging. For this reason, a scaled-up experiment was envisioned specifically for studying the wedge aerodynamics. It uses an existing high-aspect-ratio rectangular nozzle to simulate the flow over a portion of the fan annulus, as illustrated in Fig. 5. For the present experiments, the nozzle was configured to a height  $H = 17.8$  mm and width  $W = 65.0$  mm. We conducted experiments at a variety of nozzle pressure ratios (NPR) =  $p_0/p_a$ , but this paper is confined to the results for NPR = 1.6. The corresponding fully expanded exit Mach number and velocity were  $M_\infty = 0.85$  and  $U_\infty = 272$  m/s.

The flaps used to make up the wedge-shaped deflector had length  $L = 50.0$  mm and height  $h = 28.0$  mm. The flap thickness was  $t = 0.89$  mm. The perforation shapes comprised round holes (hole aspect ratio AR = 1.0) with a diameter of 2.0 mm and streamwise slots with a height of 2.0 mm and AR = 3.0. The slots had rectangular cross sections with ends that were capped off with semicircles. Examples of these flaps are shown in Fig. 6. The geometric porosity of all the flaps was  $\beta = 0.5$ . Defining  $D$  as the hole size on the plane of the freestream, the increase in AR from 1.0 to 3.0 results in a decrease in the thickness to hole size ratio  $t/D$  from 0.45 to 0.15. The flaps were inserted into slots machined into an extension of the nozzle lower wall with the wedge apex situated 20 mm downstream of the nozzle exit. The slots enabled wedge half-angles  $\alpha = 20, 30,$  and  $40$  deg.

### B. Mean Wake Surveys

The mean total pressure in the wake of the wedge was surveyed using a pitot rake system (Fig. 5). The rake consists of five 70-mm-long probes with 0.5 mm internal diameters. The probes are mounted on a streamlined holder and are spaced apart by 10 mm. Each pitot probe is connected individually to a pressure transducer (Setra Model 207). The rake is attached to a three-dimensional (3-D) traverse system consisting of three motor drivers connected individually to linear-motion guide actuators. The traverse system is controlled remotely using National Instruments LabView. The pitot rake scanned five axial planes ( $x/L = 0.5, 1.0, 1.5, 2.5,$  and  $3.5$ ) measured from the wedge apex. The scan was continuous in the spanwise ( $z$ ) direction and incremental in the transverse ( $y$ ) direction with increments  $\Delta y = 1.0$  mm. Note that the first axial station was inside the wedge. The positions  $y/L = 0.0$  and  $z/L = 0.0$  correspond to the vertical and spanwise centerplanes of the nozzle, as defined in Fig. 5. Past computations on solid FFD wedges have shown that the flow angularity at the measurement locations was typically less than 20 deg [16]. At these shallow angles, the error in the pitot measurement due to misalignment is less than 1% [18]. Further, our present computations indicate that the pressure coefficient  $C_p$  in the wake of the porous wedge does not depart

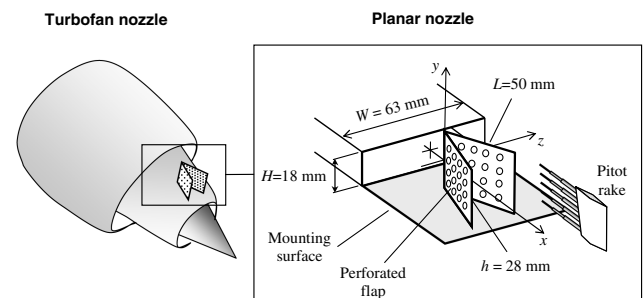


**Fig. 5** Schematic of the experiment.

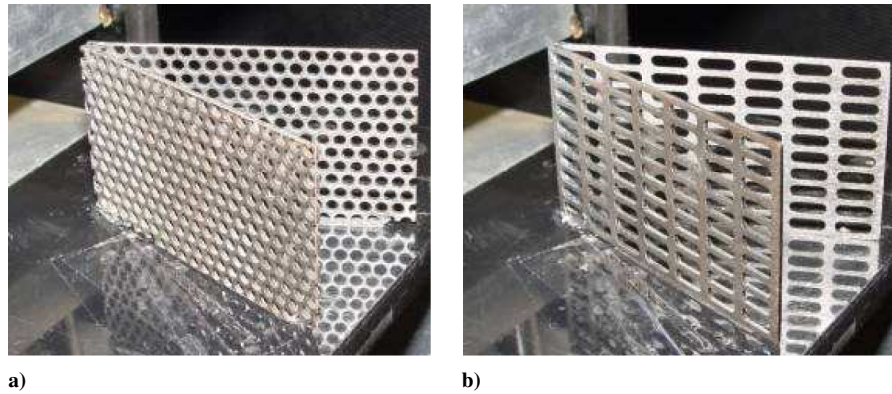


Fig. 6 Experimental perforated flaps with a) AR = 1.0 holes, and b) AR = 3.0 holes.

significantly from  $C_p = 0$  (ambient pressure), the largest deviation being around  $-0.03$ . The resulting maximum error in the Mach number inferred by the pitot measurement is 5% when the Mach number is near 0.5 (base) and 1% when the Mach number is near 0.8 (freestream).

The pressure data on each  $y$ - $z$  plane were interpolated on a fixed grid using an inverse distance weighting method. The total pressure field was converted to velocity field under the assumption of constant static pressure (equal to the ambient value) and constant total temperature (equal to room temperature). This is a reasonable assumption in the case of an FFD wedge because the top side of the wedge is exposed to ambient pressure. In the limited regions where recirculating flow was present, the pitot probe measured a very small negative pressure approximately equal to the local static pressure. In these regions, the velocity was set to zero during post processing.

### III. Computational Methods

#### A. Numerical Scheme

The computational fluid dynamics code used here solves the unsteady (3-D) Reynolds-averaged Navier–Stokes (RANS) equations on structured multiblock grids using a cell-centered finite-volume method with a Jameson–Schmidt–Turkel dissipation scheme [19]. The governing equations are solved explicitly in a coupled manner using a five-stage Runge–Kutta scheme toward steady state with local time stepping, residual smoothing, and multigrid techniques for convergence acceleration. A complete description of the computational code and numerical method can be found in [20,21]. The RANS equations were solved using the  $k$ - $\omega$  shear stress transport (SST) turbulence model. The SST model has been calibrated for separated flows and combines the advantages of  $k$ - $\omega$  and  $k$ - $\epsilon$  turbulence models to give superior performance in simulating both the wall boundary layers and free shear flows. Only the steady-state solution was considered because we are interested in the time-averaged features of the flow. A low ambient Mach number ( $M_a = 0.05$ ) with preconditioning was applied to the computational domain to prevent numerical singularities.

The computational domain is depicted in Fig. 7. The inflow boundary starts in the nozzle reservoir and the jet exit boundary extends to  $x/L = 24.0$  downstream of the nozzle exit. The lateral and transverse boundaries are located at  $z/L = 4.6$  and  $y/L = \pm 3.6$  from the nozzle center. Because there is symmetry across the wedge apex in the lateral direction, it was only necessary to compute half of the domain. For the nozzle flow, uniform total pressure was specified at the inlet surface. For the ambient lateral and transverse boundaries, a characteristic boundary condition was defined, and the downstream static pressure was fixed to ambient pressure. An adiabatic no-slip boundary condition was used on all solid walls.

The computations simulated the experimental conditions of the previous section, except for the details of the perforations. Two distinct sets of computations were performed. The first involved direct computations of physical flaps with simplified (coarse) perforations. These were used as an investigative tool to identify

salient trends in the detailed flow through the flaps that could not be observed in experiments. The second set of computations simulated the effect of the perforated flaps artificially using a body force term in the momentum equation. The formulation of the body force term is based on trends established from the first set of computations. Implementation of the body force model reduced the computational time from eight to two days using a five-node Linux cluster based on Intel 2.83 GHz quad cores.

#### B. Direct Computation of Simplified Perforations

The purpose of these computations was to provide a direct assessment of the aerodynamics of perforations. Because the cost of computing the hundreds of perforations on the experimental flaps is enormous, we simplified the geometries to very coarse perforations having about 10 holes per flap. The angle, porosity, ratio of thickness to hole size, and hole aspect ratio were similar to the experimental values. Figure 8 depicts the 3-D computational geometries. The coarse perforations required a total of approximately 10 million grid points, with about 31,000 grid points representing each hole. The grids were clustered all along the wall boundaries. We investigated computational 3-D wedges with half-angles  $\alpha = 20, 30,$  and  $40$  deg. The thickness to hole size ratio took the values  $t/D = 0.15$  (AR = 1) and  $t/D = 0.45$  (AR = 3).

The direct computations provide the wake mean flowfield that can be compared with the experimental surveys and, importantly, the detailed aerodynamics of the perforations that are impossible to probe experimentally. The latter is significant for quantifying the separation phenomena conjectured in Fig. 2. To obtain additional data on the flow through the perforations, but at a lower computational cost, we investigated 2-D wedges with  $\alpha = 20, 30,$  and  $60$  deg;  $t/D = 0.10, 0.15, 0.25, 0.45, 0.50, 1.00,$  and  $1.50$ . The porosity of each perforated wedge was  $\beta = 0.5$  with a total of 12 holes.

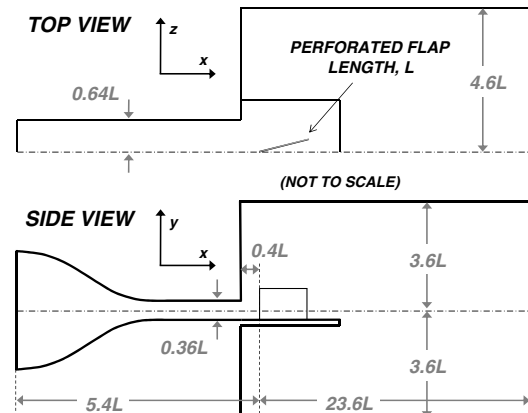


Fig. 7 Computational domain.

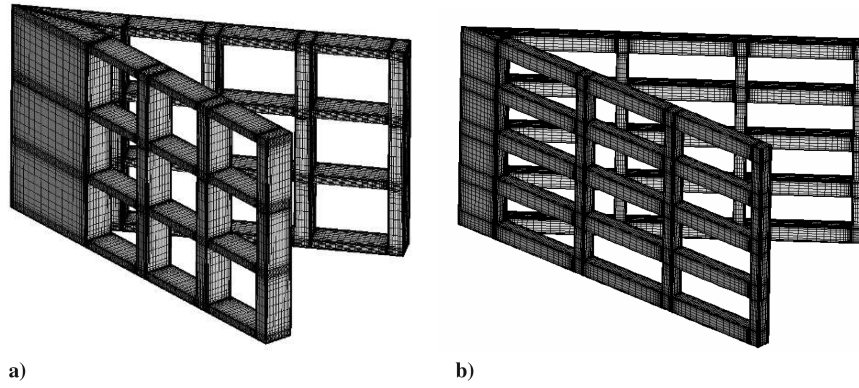


Fig. 8 Computational wedges with simplified geometries: a) AR  $\approx$  1.0; b) AR  $\approx$  3.0.

### C. Simulation Using Body Force Term

The effect of a perforated surface can be modeled by implementing a body force term in the Navier–Stokes equations:

$$\frac{\partial(\rho\mathbf{u})}{\partial t} + \nabla \cdot (\rho\mathbf{u}\mathbf{u}) = -\nabla_p + \nabla \cdot \boldsymbol{\tau} - \mathbf{F}_B \quad (2)$$

The  $\mathbf{F}_B$  term is applied locally at each cell over the entire perforated surface and generates a momentum sink that corresponds to a pressure drop across the boundary. The pressure drop across a perforated medium can be represented by the sum of a viscous loss term proportional to the local normal or permeation velocity  $\mathbf{v}_n$  and an inertial loss term proportional to the square of the permeation velocity [22–24]. The Reynolds numbers of the flows considered here are sufficiently high to justify neglecting the viscous loss term, resulting in the formulation

$$\mathbf{F}_B = \frac{1}{2} \rho C |\mathbf{v}_n| \mathbf{v}_n \quad (3)$$

where  $C$  is a dimensional coefficient called the inertial resistance coefficient. Because the body force is applied only locally, at the cells of the simulated perforated surface, it does not produce a net change in the energy balance. Therefore, the energy equation is not affected by the application of this body force. The computation involves an iterative approach, starting with an initial distribution of  $\mathbf{v}_n$  and progressively refining it until the conservation equations are satisfied. The computational mesh contained approximately 6.5 million grid points, with clustering along the wall boundaries. The rectangular grid topology used to simulate the flaps is shown in Fig. 9. Grid independence was evaluated by decreasing the spatial resolution by 50% in each axis. Comparisons of results using a fine and coarse grid will be shown in Sec. IV.C.

For a normal perforated plate, we assume that the mean flowfield is governed by the geometric porosity  $\beta$  [16] and, thus, set  $C = C(\beta)$ . We determine  $C(\beta)$  by calibrating the model against the drag coefficient measurements of Castro [10]. A 2-D Cartesian grid was used with points clustered in the vicinity of surface where the body force model was applied. Figure 10 plots the resulting resistance coefficient versus porosity. The drag coefficient results of Fig. 1 show that the calibrated model reproduces well the reduction of  $C_D$  versus  $\beta$ . The body force model mathematically breaks down as  $\beta \rightarrow 0$  because the inertial resistance coefficient becomes unbounded to counter the effect of the permeation velocity approaching zero. In practice, a reasonable numerical prediction of the solid boundary case can be obtained by setting  $C$  to a sufficiently large value.

For the computation of inclined perforations, the approach was to use the normal-plate calibration, but in terms of an effective porosity that accounts for the blockage of the separation bubble discussed in Sec. I.B. From the sketch of Fig. 2 and the conjecture of Eq. (1), the ratio of effective to geometric porosity is

$$\frac{\beta_{\text{eff}}}{\beta} = 1 - \frac{s}{D} = 1 - \cos^n \alpha \tanh \left[ b \frac{t}{D} \right] \quad (4)$$

The constants  $n$  and  $b$  are to be determined by examining the behavior of the separation bubble from the RANS computations on the simplified perforations. Once a model for  $\beta_{\text{eff}}$  is established, we use  $C(\beta_{\text{eff}})$  in the body force model based on the normal-plate calibration.

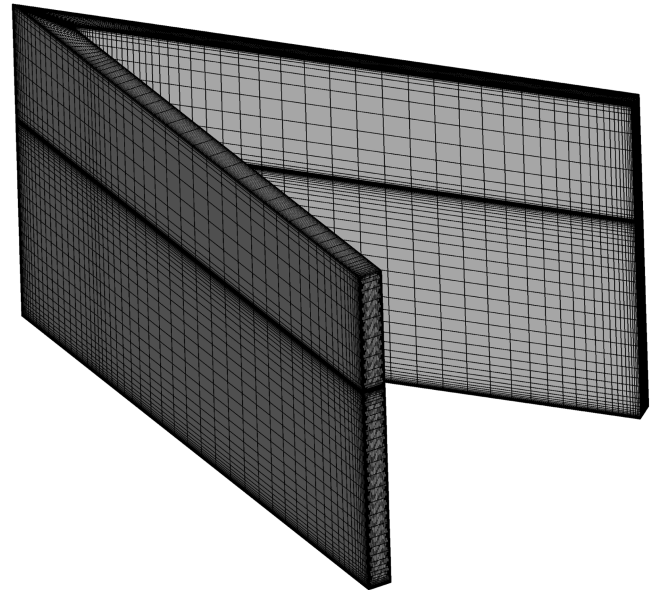


Fig. 9 Computational grid of the wedge used with the body force model.

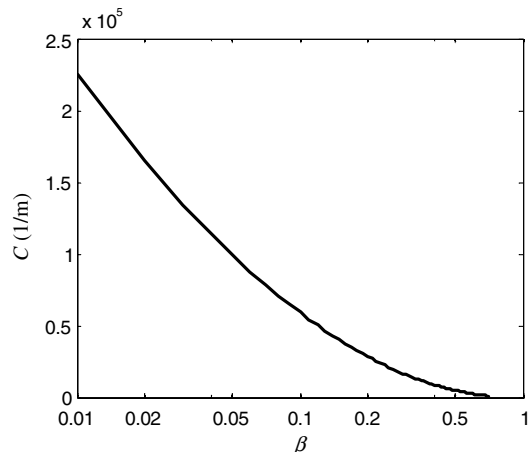


Fig. 10 Inertial resistance coefficient for a porous plate normal to a freestream.

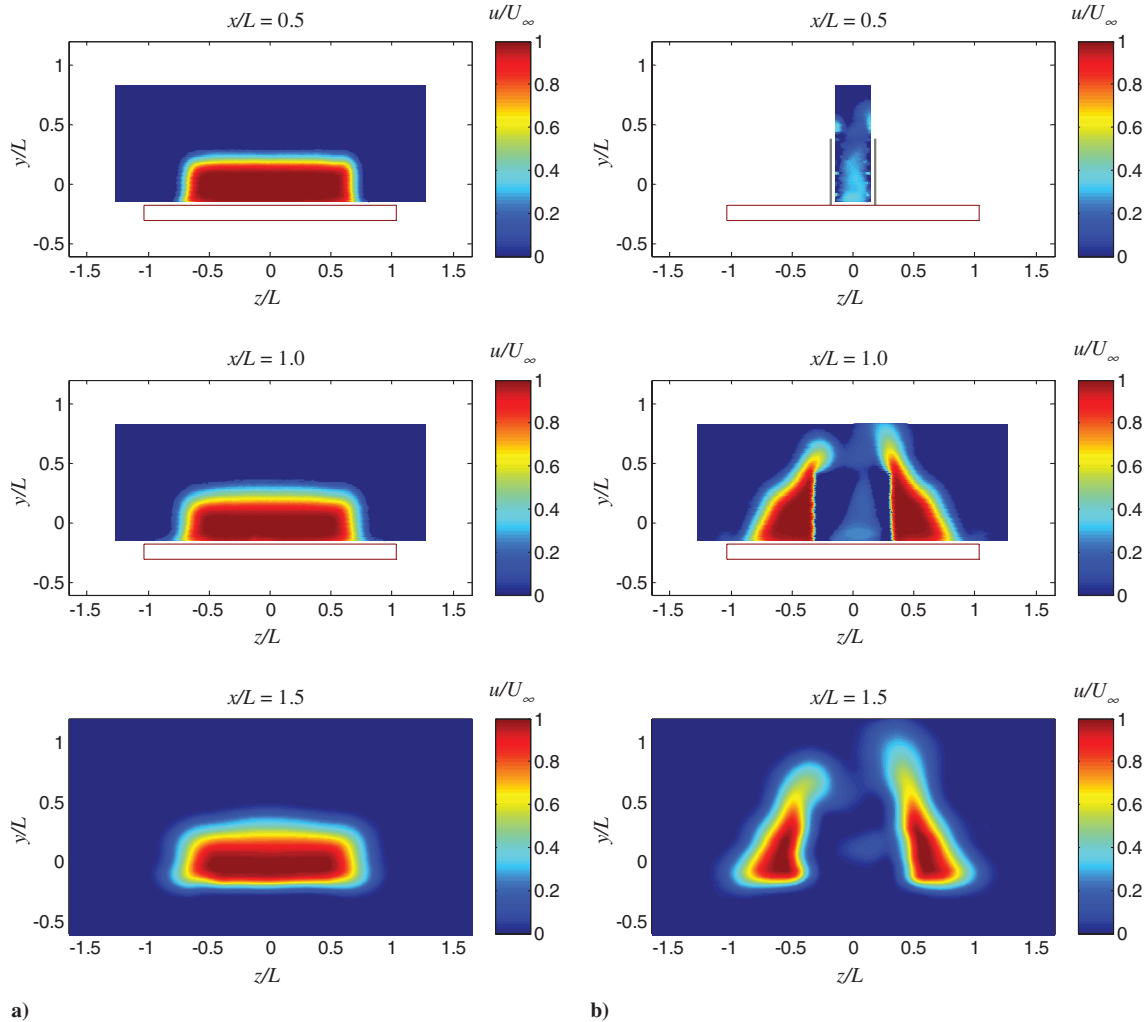


Fig. 11 Mean axial velocity contours at the first three axial stations: a) no flaps, b) flaps with  $\beta = 0.5$ , and  $\alpha = 20$  deg.

## IV. Results

### A. Experimental Results

We begin the presentation of the experimental results with the mean flowfield of the rectangular jet without the wedge. Mean axial velocity contours at the first three axial stations are shown in Fig. 11a. The mean velocity has been normalized by the perfectly expanded jet exit velocity  $U_\infty$ . The first axial station is located  $0.9L$  from the exit of the nozzle, corresponding to  $x/L = 0.5$  from where the apex of the wedge would be located. The flow develops normally downstream with mixing primarily occurring on the upper and side boundaries due to the confinement of the jet by the lower wall surface in the near field. The boundary layer on the mounting wall surface was not resolved in these experiments because the tapered structure of the pitot probes prevents their tips from coming very close to the surface. The potential core of the jet extends downstream a distance of  $3.2L$  from the nozzle exit.

Considering now the flow with perforated flaps, Fig. 11b plots the mean velocity contours for  $\alpha = 20$  deg,  $AR = 1.0$  (round holes) and  $t/D = 0.45$ . We observe strong sideward deflections and the upwash mentioned in Sec. I.C. The flow bled through the perforations coalesces into a centered jet rather than spreading uniformly. The jet at the wedge base is fairly weak, indicating strong blockage for this configuration. We found the flowfield to be very sensitive to small asymmetries in the configuration of the flaps, and we were not able to establish a perfectly symmetric mean flowfield. We do not expect departures from symmetry to affect the key results of this study.

We now investigate two distinct changes relative to the configuration of Fig. 11b: increasing the wedge angle  $\alpha$  and increasing the hole aspect ratio  $AR$ . The effect of increasing  $\alpha$  from 20 to 30 deg is captured in Fig. 12a. Comparing with the same axial station ( $x/L = 1.0$ ) of Fig. 11b, we note a stronger jet at the wedge base, with the base flow remaining highly nonuniform. Increasing the

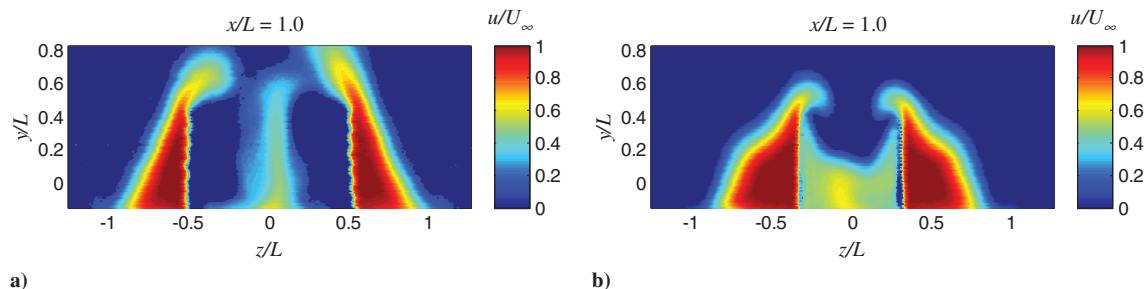


Fig. 12 Mean axial velocity contours at the wedge base  $\beta = 0.5$  and a)  $AR = 1.0$ ,  $\alpha = 30$  deg; b)  $AR = 3.0$ ,  $\alpha = 20$  deg.

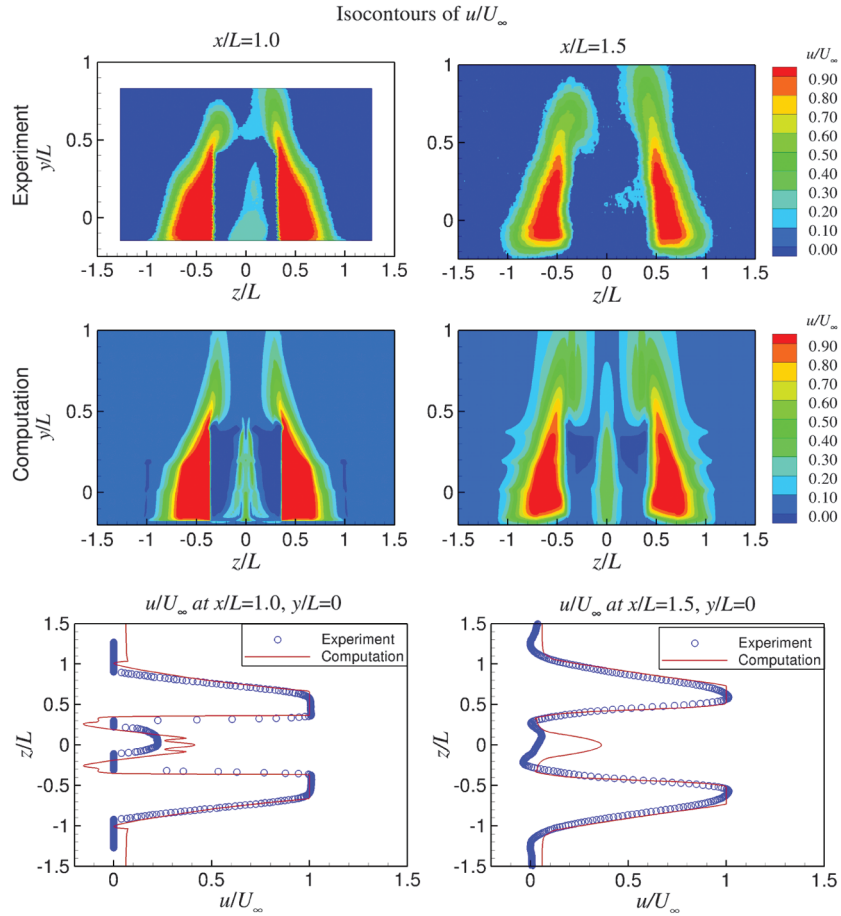


Fig. 13 Comparison of experimental and direct computational results for  $\beta = 0.5$  ( $\alpha = 20$  deg,  $AR = 1.0$ ).

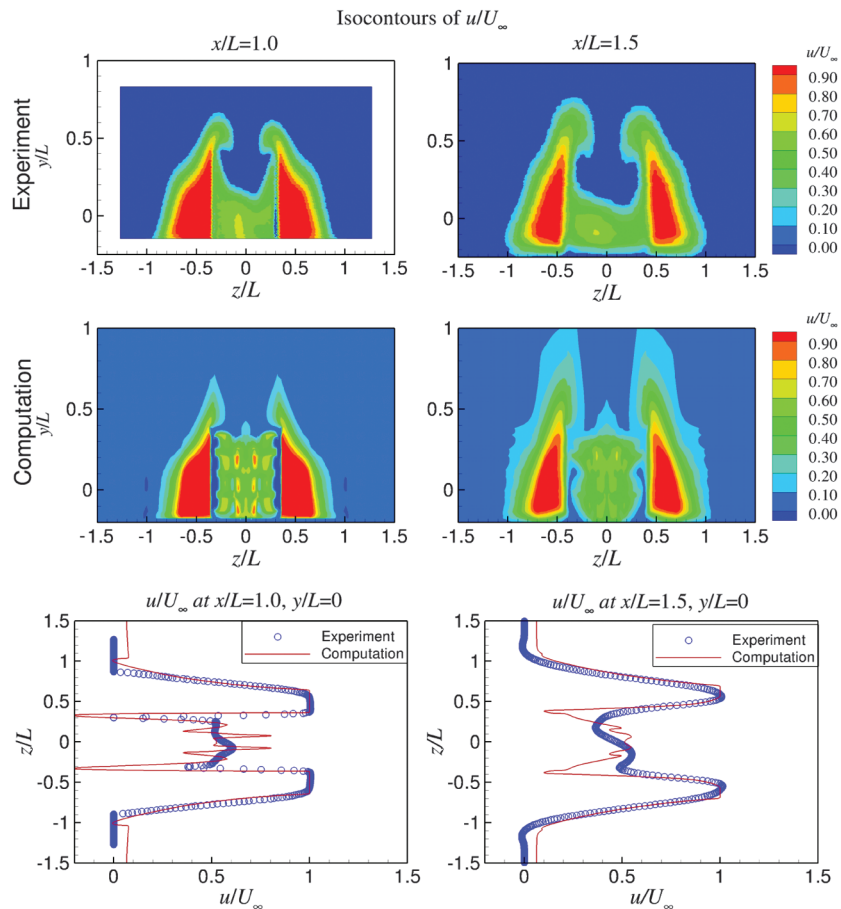


Fig. 14 Comparison of experimental and direct computational results for  $\beta = 0.5$  ( $\alpha = 20$  deg,  $AR = 3.0$ ).

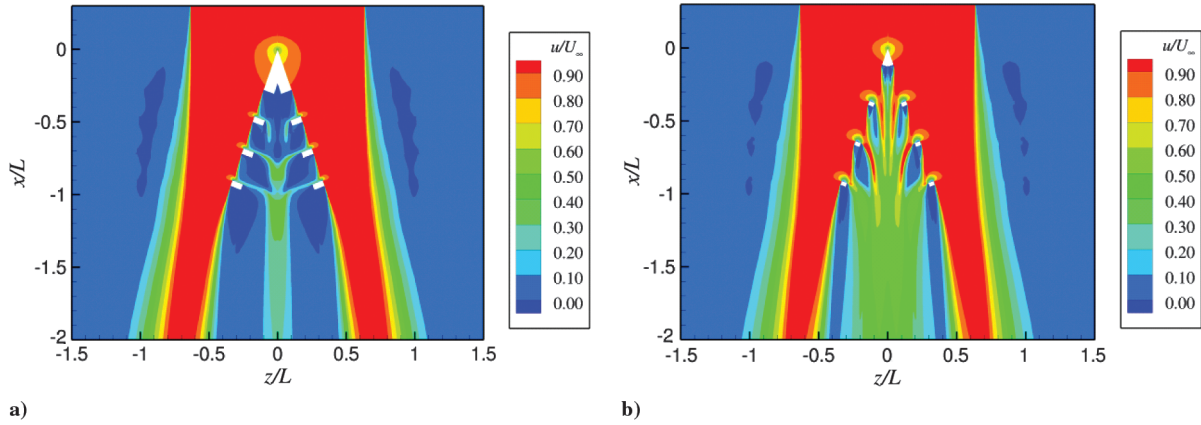


Fig. 15 Computational mean axial velocity on the  $x$ - $z$  plane for  $\beta = 0.5$ ,  $\alpha = 20$  deg; and a)  $AR = 1.0$ , and b)  $AR = 3.0$ .

hole aspect ratio from  $AR = 1.0$  to  $3.0$  while maintaining  $\alpha = 20$  deg, Fig. 12b, results in a much fuller base flow and less of an upwash. The trends illustrated by Fig. 12 were also observed for other wedge half-angles and nozzle pressure ratios. These comparisons indicate substantially different flowfields at the same geometric porosity  $\beta$  and underscore the importance of defining an effective porosity for the treatment of this flow.

**B. Computations of Simplified Perforations**

The RANS computations on simplified perforations were performed at approximately the same porosity, angles, thickness to hole diameter ratios, and hole aspect ratios of the experiments. The numerical results provide detailed information on the flowfield through the perforations that cannot be resolved in the experiments. To assess the fidelity of the computations, we compare predicted and

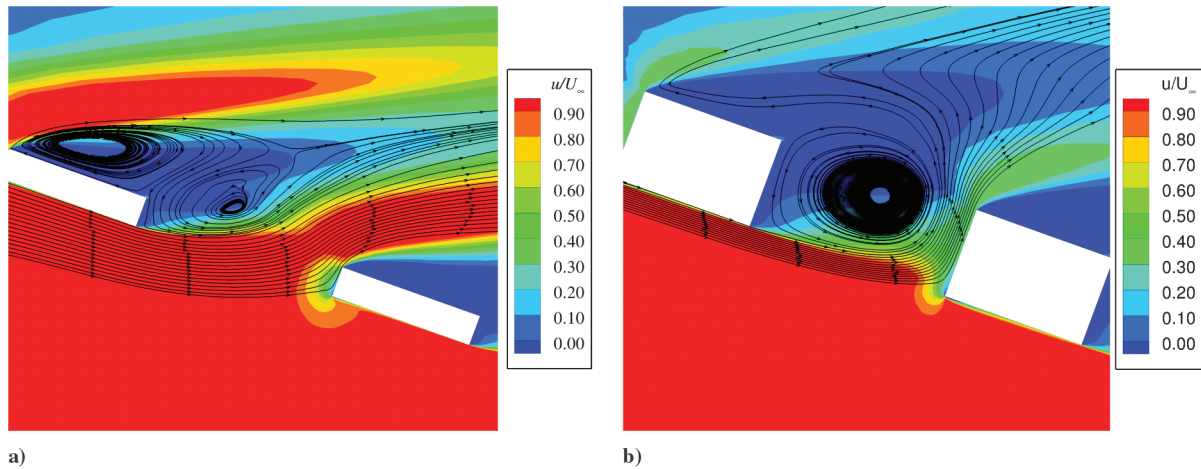


Fig. 16 Comparison of 2-D computations for  $\beta = 0.5$ ,  $\alpha = 20$  deg; and a)  $t/D = 0.15$ , and b)  $t/D = 0.45$ .

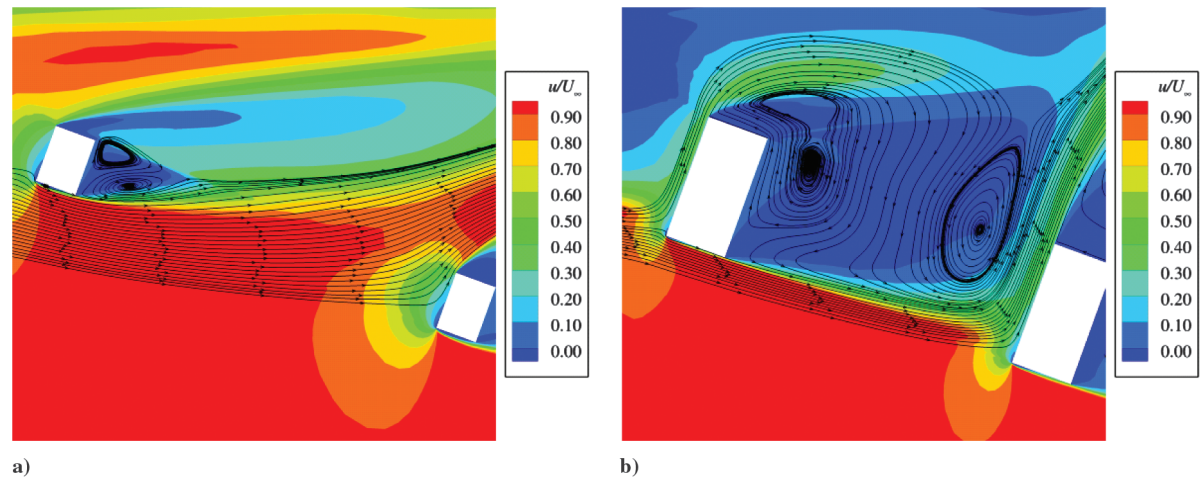
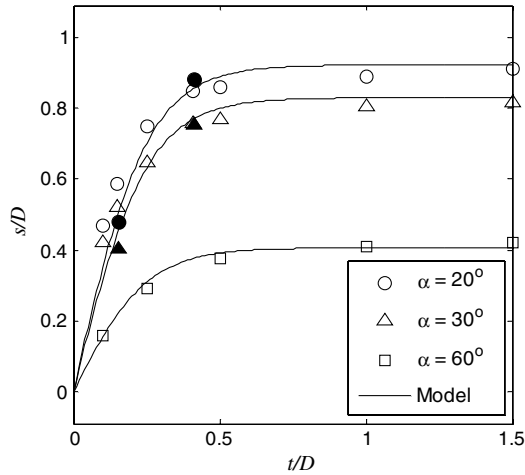


Fig. 17 Comparison of 3-D computations for  $\beta = 0.5$ ,  $\alpha = 20$  deg; and a)  $AR = 1.0$  ( $t/D = 0.15$ ); b)  $AR = 3.0$  ( $t/D = 0.45$ ).



**Fig. 18** Comparison of model prediction with computed values of separation bubble size; solid symbols represent 3-D configurations.

measured mean flow profiles in Figs. 13 and 14 for  $AR = 1.0$  and  $3.0$ , respectively. Although the computational perforations are much coarser than the experimental perforations, the same flow trends are observed. In particular, we note the increase in wake velocity with increasing  $AR$ .

We now examine the respective computational velocity fields on the  $x$ - $z$  mid plane of the wedge, shown in Fig. 15. For  $AR = 1.0$  ( $t/D = 0.45$ ), there is significant blockage of flow through the perforations. The primary driver of flow penetration through the surface is the pressure difference across the flap. For  $AR = 3.0$  ( $t/D = 0.15$ ), there appears to be a direct flowpath through the surface with minimal blockage. Understanding the nature of the flow

blockage requires a closer inspection of the flow pattern near a given hole. We study the flowfields through 2-D and 3-D perforated flaps, the latter corresponding to the results just presented above. Figure 16 compares the flowfields of 2-D perforated wedges with equal porosity and half-angle, but varying thickness to hole diameter ratio. For the thinner wedge shown in Fig. 16a there is little blockage, and the flow passes directly through the perforation. For the thicker wedge in Fig. 16b, a separation bubble forms within each hole that significantly constricts the passage of flow through the surface. Because the separated regions effectively act as solid surfaces, the effective porosity of the thicker wedge is smaller than that of the thinner wedge, even though the geometric porosity remains the same. Figure 17 shows a similar comparison for simplified 3-D wedges. The structure of the separation bubble becomes 3-D with the introduction of transverse flow (upwash) along the wedge face. However, the general trends observed in the 2-D computations are still retained.

The results exemplified by Figs. 16 and 17 enable us to calculate the separation bubble size  $s$  and build the model discussed in Sec. I.B. The bubble size is determined by following the separation streamline originating at the upstream corner of the perforation until its displacement from the downstream edge is a minimum, as shown in Fig. 2. For 3-D computations, this value is averaged over the transverse extent of each hole. While the bubble size is approximately the same from hole to hole along the length of the flap, there is an appreciable change in bubble size between holes in the  $y$  direction for the 3-D configurations. For this reason, the average bubble size over the entire flap is calculated to give a characteristic separation thickness for each geometric configuration. The normalized bubble size  $s/D$  is plotted versus the normalized thickness  $t/D$  in Fig. 18 for several wedge half-angles and thickness ratios. Both 2-D and 3-D computational results are shown by the symbols. The solid lines represent the model of Eq. (4) with coefficients  $n = 1.3$  and  $b = 4.0$ . The agreement between the model

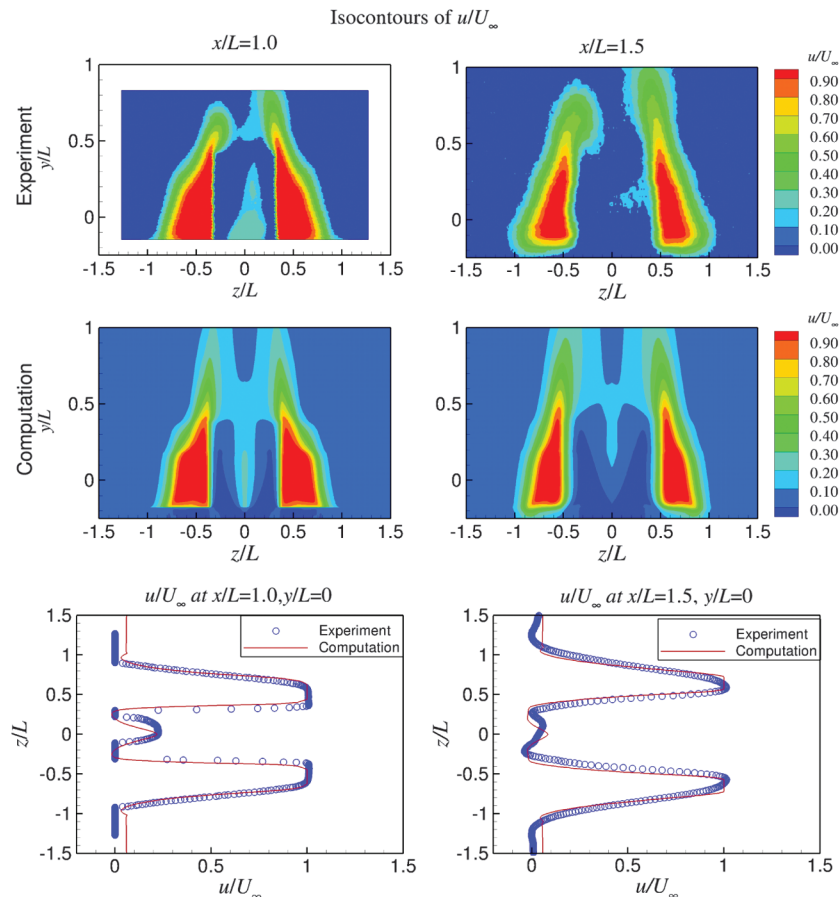


**Fig. 19** Comparison of experimental and body force computational results for  $\beta = 0.5$  ( $\alpha = 20$  deg,  $AR = 1.0$ ).

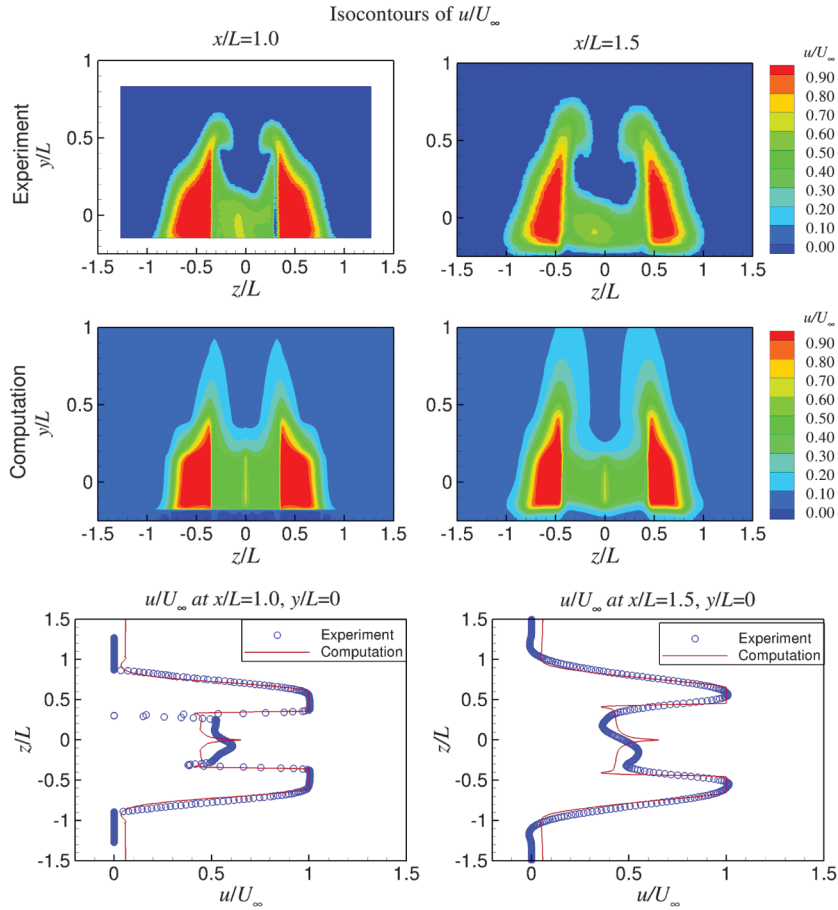


Fig. 20 Comparison of experimental and body force computational results for  $\beta = 0.5$  ( $\alpha = 20$  deg,  $AR = 3.0$ ).

curves and the computational results is reasonable for both 2-D and 3-D configurations.

C. Body Force Model Formulation and Validation

Having established reasonable parameters for the effective porosity model of Eq. (1) in the form

$$\frac{\beta_{\text{eff}}}{\beta} = 1 - \frac{s}{D} = 1 - \cos^{1.3} \alpha \tanh \left[ 4 \frac{t}{D} \right] \quad (5)$$

the inertial resistance coefficient of an inclined perforation is now known in terms of  $C(\beta_{\text{eff}})$ , with the function  $C$  having been determined from the normal-plate drag results of Castro [10]. The body force model of Eq. (3) is now complete, and we are able to conduct RANS simulations of the wedge flaps without resolving the individual perforations.

We present results of the computations with body force for wedge flaps with half-angle  $\alpha = 20$  deg, porosity  $\beta = 0.5$ , and hole aspect

ratios  $AR = 1.0$  and  $3.0$  ( $t/D = 0.45$  and  $0.15$ , respectively). Figure 19 compares experimental and computational mean velocity results for the  $AR = 1.0$  configuration. The computation reproduces well the external shear layer and the internal flowfield, including the coalescence of the internal flow into a narrow jet. The computation also captures the upwash, although the detailed structure of the upwash is somewhat different. Note that the computation was done with a small forward Mach number, which could impact the evolution of the upwash. Figure 20 presents the analogous comparisons for the  $AR = 3.0$  case. Again, there is very good reproduction of the external and internal flows, including the weaker upwash and stronger, more uniform flow at the wedge base. Grid independence was evaluated by reducing the number of grid points to 12.5% of the original grid (50% reduction in each spatial direction). The comparison of velocity profiles is shown in Fig. 21. The changes are negligible, indicating adequate grid resolution. The prediction of the base flow is critical for the successful implementation of the FFD wedge noise reduction scheme. It appears that the body force model,

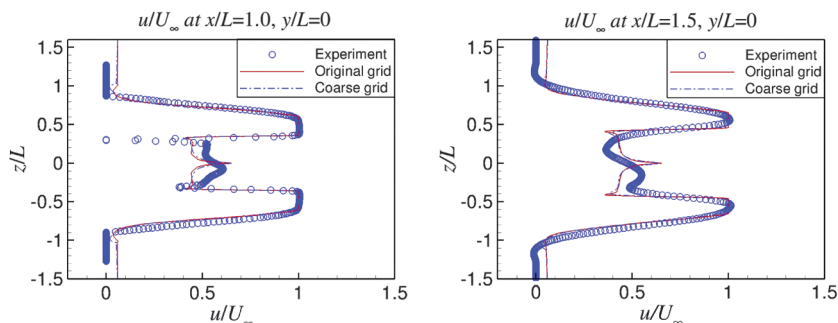


Fig. 21 Comparison of velocity profiles between different grids for  $\beta = 0.5$  ( $\alpha = 20$  deg,  $AR = 3.0$ ).

which cuts down computational costs dramatically, is a satisfactory design tool for the engineering of these devices.

We note that the computations were conducted with a small forward Mach number, which explains subtle differences in the background colors of the velocity contour maps in Figs. 19 and 20. We also wish to point out that the effects of skin friction have been neglected in our body force modeling. Based on drag measurements on perforated acoustic liners [25] and the results of the present computations, we estimate that skin friction drag is at least one order of magnitude lower than pressure drag for wedge half-angles of 20 deg or higher [26]. Therefore, we expect that skin friction will not significantly affect the aerodynamic performance unless the wedge angle is very small.

## V. Conclusions

Experiments and computations were used to investigate the aerodynamics of perforated plates inclined to a freestream, with emphasis on wedge-shaped deflectors used for jet noise reduction in turbofan engines. The study comprised plates with same geometric porosity and different inclination angles and hole aspect ratios. Compared to the case of normal incidence, the inclination angle causes more flow blockage. The blockage is connected to flow separation inside each perforation hole, which was studied extensively by the computations. A simple model for the separation bubble size, calibrated by the computational results, enables the definition of an effective porosity of the inclined plate. The effective porosity is then used in a body force model that obviates resolution of the individual perforations and produces mean flow predictions that agree well with the experiments. For fixed plate thickness, angle, and geometric porosity, the effective porosity can be increased by elongating the holes (increasing their aspect ratio) in the direction of the incident flow. For the case of the wedge deflector, this approach is shown to produce a full and uniform base flow: an important characteristic for the successful implementation of the wedge for jet noise suppression. More broadly, the computational body force model is shown as a promising engineering tool for a large class of problems involving normal and angled perforations.

The main limitation of the present model is the omission of skin friction on the porous surface. As pointed out earlier, skin-friction drag is estimated to be an order of magnitude lower than pressure drag for inclination angles of 20 deg and higher. To extend the model to smaller inclination angles, the body force term needs to be revised to include the effects of skin friction. These effects can be evaluated using direct computations on coarse perforations, as was done in the present study, then included appropriately in a body force model.

## Acknowledgment

The support by NASA Cooperative Agreement NNX07AC62A (monitored by K. B. M. Q. Zaman) is gratefully acknowledged.

## References

- [1] Purser, P. E., and Turner, T. R., "Aerodynamic Characteristics and Flap Loads of Perforated Double Split Flaps on a Rectangular NACA 23012 Airfoil," Langley Memorial Aeronautical Lab., Langley Field, VA, War-time Rept. B810608, 1943.
- [2] Sakaliyski, K. D., Hileman, J. I., and Spakovszky, Z. S., "Aero-Acoustics of Perforated Drag Plates for Quiet Transport," AIAA Paper 2007-1032, Jan. 2007.
- [3] Nedic, J., Ganapathisubramani, B., Vassilicos, J. C., Boree, J., Brizzi, L. E., and Spohn, A., "Aero-Acoustic Performance of Fractal Spoilers," AIAA Paper 2011-1084, 2011.
- [4] Lee, T., "Aerodynamic Characteristics of Airfoil with Perforated Gurney-Type Flaps," *Journal of Aircraft*, Vol. 46, No. 2, 2009, pp. 542–548.  
doi:10.2514/1.38474
- [5] Staelens, Y. D., Blackwelder, R. F., and Page, M. A., "Study of Belly-Flaps to Enhance Lift- and Pitching Moment Coefficient of a BWB-Airplane," AIAA Paper 2007-4176, June 2007.
- [6] Clark, R. L., "Weapons Bay Turbulence Reduction Techniques," Air Force Flight Dynamics Lab., Wright Patterson AFB, OH, TM-75-147-FXM, Dec. 1975.
- [7] Papamoschou, D., "Pylon Based Jet Noise Suppressors," *AIAA Journal*, Vol. 47, No. 6, 2009, pp. 1408–1420.  
doi:10.2514/1.37780
- [8] Ranga Raju, K. G., Garde, R. J., Singh, S. K., and Singh, N., "Experimental Study on Characteristics of Flow Past Porous Fences," *Journal of Wind Engineering and Industrial Aerodynamics*, Vol. 29, Nos. 1–3, 1988, pp. 155–163.  
doi:10.1016/0167-6105(88)90154-7
- [9] Fried, E., and Idel'chik, I. E., *Flow Resistance: A Design Guide for Engineers*, Hemisphere, London, 1989, Chap. 8.
- [10] Castro, I. P., "Wake Characteristics of Two-Dimensional Perforated Plates Normal to an Airstream," *Journal of Fluid Mechanics*, Vol. 46, No. 3, 1971, pp. 599–609.  
doi:10.1017/S0022112071000727
- [11] Shiau, S., "Measurement of Turbulence Characteristics for Flow Past Porous Windscreen," *Journal of Wind Engineering and Industrial Aerodynamics*, Vols. 74–76, 1998, pp. 521–530.  
doi:10.1016/S0167-6105(98)00047-6
- [12] Lee, S.-J., and Kim, H.-B., "Laboratory Measurements of Velocity and Turbulence Field Behind Porous Fences," *Journal of Wind Engineering and Industrial Aerodynamics*, Vol. 80, No. 3, 1999, pp. 311–326.  
doi:10.1016/S0167-6105(98)00193-7
- [13] Kim, H.-B., and Lee, S.-J., "Hole Diameter Effect on Flow Characteristics of Wake Behind Porous Fences Having the Same Porosity," *Fluid Dynamics Research*, Vol. 28, No. 5, 2001, pp. 311–326.  
doi:10.1016/S0169-5983(00)00036-8
- [14] Papamoschou, D., "Fan Flow Deflection in Simulated Turbofan Exhaust," *AIAA Journal*, Vol. 44, No. 12, 2006, pp. 3088–3097.  
doi:10.2514/1.22552
- [15] Papamoschou, D., Vu, A., and Johnson, A., "Aerodynamics of Wedge-Shaped Deflectors for Jet Noise Reduction," AIAA Paper 2006-3655, June 2006.
- [16] Xiong, J., Liu, F., and Papamoschou, D., "Computation of the Flow of a Dual-Stream Jet with External Solid and Perforated Wedge Deflectors for Noise Reduction," AIAA Paper 2010-4863, July 2010.
- [17] Von Tanner, M., "Determination of Base Drag with Application to Near Wake of Wedges," *Mitteilungen aus dem Max-Planck Institut für Strömungsforschung und der Aerodynamischen Versuchsanstalt*, No. 31, 1964.
- [18] Liepmann, H. W., and Roshko, A., *Elements of Gas Dynamics*, Wiley, New York, 1957, pp. 147–149.
- [19] Jameson, A., Schmidt, W., and Turkel, E., "Numerical Solution of the Euler Equations by Finite Volume Methods Using Runge-Kutta Time-Stepping Schemes," AIAA Paper 1981-1259, June 1981.
- [20] Xiong, J., Nielsen, P. E., Liu, F., and Papamoschou, D., "Computation of High-Speed Coaxial Jets with Fan Flow Deflection," *AIAA Journal*, Vol. 48, No. 10, 2010, pp. 2249–2262.  
doi:10.2514/1.J050331
- [21] Liu, F., and Zheng, X., "A Strongly Coupled Time-Marching Method for Solving the Navier–Stokes and  $k-\omega$  Turbulence Model Equations with Multigrid," *Journal of Computational Physics*, Vol. 128, No. 2, 1996, pp. 289–300.  
doi:10.1006/jcph.1996.0211
- [22] Sozer, E., Shyy, W., and Thakur, S., "Multi-Scale Porous Media Modeling for Liquid Rocket Injector Applications," AIAA Paper 2006-5044, July 2006.
- [23] Angland, D., Zhang, X., and Molin, N., "Measurements of Flow Around Flap Side Edge with Porous Edge Treatment," *AIAA Journal*, Vol. 47, No. 7, 2009, pp. 1660–1671.  
doi:10.2514/1.39311
- [24] Forchheimer, P., "Wasserbewegung Durch Boden," *Zeitschrift des Vereines Deutscher Ingenieure*, Vol. 45, 1901, pp. 1782–1788.
- [25] Wolter, J. D., "Drag Measurements of Porous Plate Acoustic Liners," AIAA Paper 2005-0803, Mar. 2005.
- [26] Johnson, A., Xiong, J., Rostamimonjezi, S., Liu, F., and Papamoschou, D., "Aerodynamic and Acoustic Optimization for Fan Flow Deflection," AIAA Paper 2011-1156, Jan. 2011.